IOP Publishing Smart Materials and Structures
Smart Mater. Struct. **23** (2014) 085018 (17pp) doi:10.1088/0964-1726/23/8/085018

Nonlinear dynamics of a pseudoelastic shape memory alloy system—theory and experiment

S Enemark[1], M A Savi[2] and I F Santos[1]

[1] Technical University of Denmark, Department of Mechanical Engineering, DK-2800 Kongens Lyngby, Denmark
[2] Universidade Federal do Rio de Janeiro, COPPE—Department of Mechanical Engineering, 21.941.972—Rio de Janeiro—RJ—Brazil, PO Box 68.503

E-mail: soene@mek.dtu.dk, savi@mecanica.ufrj.br and ifs@mek.dtu.dk

Received 3 February 2014, revised 25 April 2014
Accepted for publication 15 May 2014
Published 2 July 2014

Abstract

In this work, a helical spring made from a pseudoelastic shape memory alloy was embedded in a dynamic system also composed of a mass, a linear spring and an excitation system. The mechanical behaviour of shape memory alloys is highly complex, involving hysteresis, which leads to damping capabilities and varying stiffness. Besides, these properties depend on the temperature and pretension conditions. Because of these capabilities, shape memory alloys are interesting in relation to engineering design of dynamic systems. A theoretical model based on a modification of the 1D Brinson model was established. Basically, the hardening and the sub-loop behaviour were altered. The model parameters were extracted from force–displacement tests of the spring at different constant temperatures as well as from differential scanning calorimetry. Model predictions were compared with experimental results of free and forced vibrations of the system setup under different temperature conditions. The experiments give a thorough insight into dynamic systems involving pseudoelastic shape memory alloys. Comparison between experimental results and the proposed model shows that the model is able to explain and predict the overall nonlinear behaviour of the system.

Keywords: dynamical systems, shape memory alloys, model validation

(Some figures may appear in colour only in the online journal)

1. Introduction

Shape memory alloys (SMAs) belong to the smart materials family and present remarkable thermo-mechanical behaviour. This behaviour includes large recoverable strains, pseudoelasticity, and hysteretic behaviour, among others. These effects are caused by phase transformations between austenitic and martensitic phases that are stable at different conditions of stress and temperature.

These capabilities have drawn increasing attention in the field of engineering design, and nowadays SMAs are found in several applications, e.g., as fibres in composite material structures for adjusting natural frequencies or shape, or for reducing vibrations (Cartmell *et al* 2012); in civil engineering for seismic isolation and energy dissipation (of cultural heritage structures); and employed as sensors, actuators, and tendons in concrete members (Janke *et al* 2005).

To be able to use SMAs for complex tasks in industrial applications, reliable models must be established, and this is still a concern in academia. Paiva and Savi (2006), Lagoudas (2008) presented a general overview related to SMA modelling.

The capabilities of SMAs in relation to dynamic systems have been investigated in distinct publications. Machado *et al* (2009), Savi *et al* (2011) and Bernardini and Rega (2011a, 2011b) investigated one degree of freedom systems with SMA suspensions numerically. In these setups, both tension and compression of the SMA elements were allowed, and the dynamic behaviours were complex, showing period-multiple orbits, quasi-periodic and chaotic motion, and

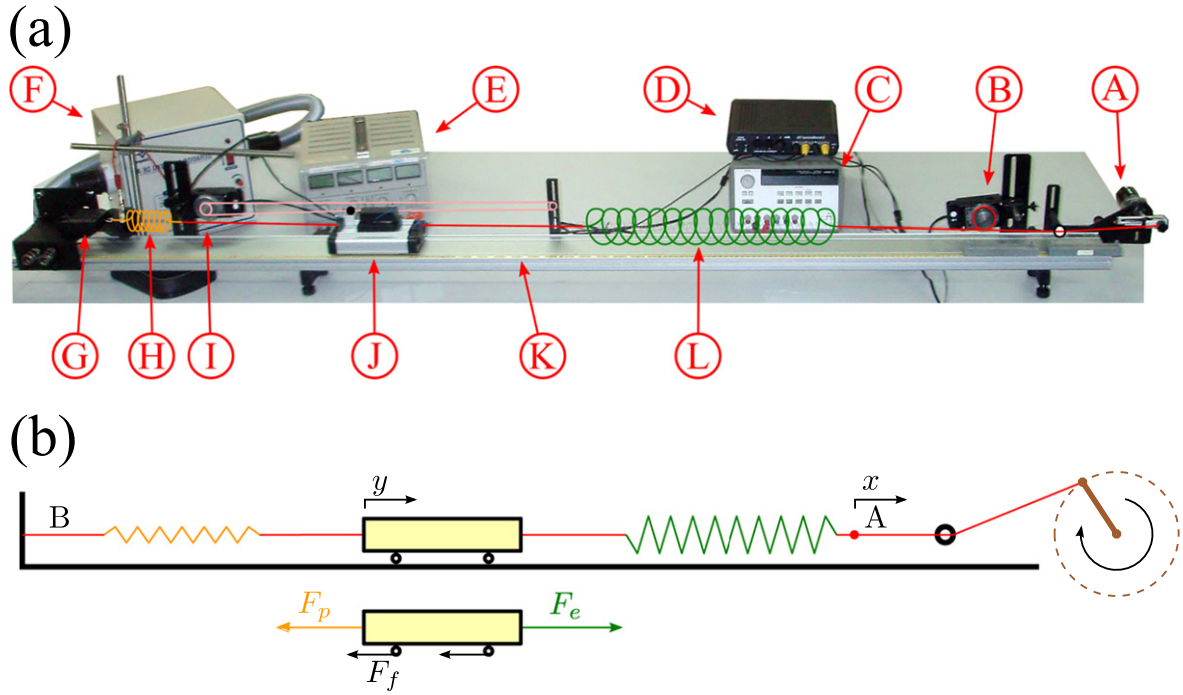

Figure 1. Test rig; picture (a) and schematics (b). (a): (A) PASCO oscillator, (B) PASCO rotary motion sensor for measuring excitation displacement, (C) power supply to oscillator, (D) PASCO receiver connected to sensors and computer, (E) power supply for heating the PE spring, (F) blower for cooling the PE spring, (G) PASCO force sensor for measuring the PE spring force, (H) PE spring, (I) PASCO rotary motion sensor for measuring the displacement of the cart, (J) PASCO cart with masses, (K) PASCO horizontal slide, (L) linear spring. Between the oscillator, springs, cart, and force sensor, nylon threads connect the elements. (b): Sketch of mechanical components to the right is an oscillator (brown) pulling a thread (red). The linear spring (green) is connected to the cart (yellow). On the left side of the cart is the pseudoelastic spring (orange). The displacement of the excitation x is measured at point A. The displacement of the cart y is measured at a separate thread connected to the cart. At point B the thread force is measured, equalling the pseudoelastic spring force. The pseudoelastic spring force is F_p, F_e is the linear elastic spring force and F_f is the friction force from the wheels of the cart.

coexisting attractors. Williams *et al* (2002) used the stiffness differences between austenite and martensite to produce an adaptive tuned vibration absorber by controlling the temperature of the SMA elements. The same principle was employed by Nagaya *et al* (1987) for passing through critical speeds in rotor-bearing systems.

Non-smooth oscillators with SMA supports have been investigated numerically by dos Santos and Savi (2009). Silva *et al* (2013) made a similar numerical analysis on a non-smooth rotor-bearing system, showing improved behaviour compared with an elastic support. Again, both tension and compression in the SMA element were allowed.

Experimental investigations of SMA systems are less common. Aguiar *et al* (2013) investigated SMA oscillator dynamics considering one and two degrees of freedom systems excited by a shaker. Different aspects of system dynamics were treated. Enemark *et al* (2014) presented an experimental investigation related to a one degree of freedom oscillator with harmonic excitation. Concerning non-smooth systems, a comparison between experiments and modelling was made by Sitnikova *et al* (2012) in the same field, where the resulting dynamic responses had complex nonlinear characteristics. Pretensioned pseudoelastic SMA elements were used.

The thermo-mechanical behaviour of helical springs is of special interest in the dynamical study of SMA systems. Studies of helical springs made from SMAs are found in literature. These studies have revealed that the stress and strain distributions in the springs can be complex (Mirzaeifar *et al* 2011, Lagoudas *et al* 2012). This is due to small spring indices and large pitch angles combined with large spring deformations. Several attempts at using simple equivalent one-dimensional models have been made, still with good resemblance to experiments (Aguiar *et al* 2010, Mirzaeifar *et al* 2011, An *et al* 2012).

This paper deals with a comparison between theory and experiments related to a pseudoelastic SMA system. The experimental test rig used in this work was a one degree of freedom system consisting of a mass connected to a linear spring and a pseudoelastic SMA spring. Both springs were in pretension. The linear spring was connected to a DC motor that provided a harmonic excitation to the system. The SMA was used as an active element in the system and not as an external actuator, and therefore the system behaviour greatly depended on the properties of the SMA. Different operating conditions could be induced by a change in the temperature or a change in the level of pretension of the SMA spring. Only passive control of the system dynamics has been treated. The SMA spring was pseudoelastic, meaning that phase transformation induced during loading is completely recovered during unloading. Such a spring exhibits hysteretic behaviour

Table 1. Data of the experimental setup as well as characteristic quantities. *Depending on the day the experiment was performed.

Pseudoelastic SMA spring	
Wire diameter (mm)	0.50
Coil diameter (mm)	5.6
Initial length of spring l_0 (mm)	65
Number of coils	36
Cart	
Mass m (g)	770
Linear elastic steel spring	
Stiffness k_l (N m^{-1})	3.25
Characteristic quantities (besides l_0)	
Initial stiffness of SMA spring k_0 (N m^{-1})	20
Frequency $\omega_0 = \frac{1}{2\pi}\sqrt{(k_0 + k_l)m^{-1}}$ (Hz)	0.87
Assumed current-temperature relation	
No current, 0 A	23 to 25 °C*
High current, 1.1 A	80 °C

as well as changing stiffness, and both these elements greatly affect system dynamics.

The goal of this research is to explain and predict the behaviour of a one degree of freedom dynamical system involving a pseudoelastic shape memory alloy (PE SMA) spring, and through that also to show the dynamical capabilities of such a smart material. It shows the feasibility of applying SMAs as dissipation elements and shows the potential for their adaptive behaviour to temperature, which can be controlled. Brinson's model (Brinson 1993, Brinson and Huang 1996, Bekker and Brinson 1998) was employed to describe the thermo-mechanical behaviour of the SMA spring, and two novel changes ensure better resemblance to experiments. Furthermore, direct comparison between theory and experiment is rare in this field, and in particular the investigations of equilibrium position changes due to temperature alterations are interesting.

The outline of this paper is as follows. Initially, a description of the experimental setup is presented. Theoretical modelling follows, showing the Brinson model and the proposed changes to it; then the helical spring model is discussed followed by the equations of motion of the dynamic system. Characterisation of the pseudoelastic spring is shown, and this is used in the analyses of the dynamic system in free and forced vibration for constant and varying temperatures.

2. Experimental setup

The experimental setup is a one degree of freedom SMA oscillator that consists of a cart with a mass connected to a linear spring and an SMA spring. The other end of the linear spring is connected to a 12 V DC motor that provides a harmonic excitation. The SMA helical spring is pseudoelastic, where the austenitic phase is stable at room temperature. Figure 1(a) presents a system picture, whereas a sketch of the system components is shown in figure 1(b). The experimental setup is monitored by two rotary motion sensors (PASCO encoder CI-6538 with 1,440 orifices and a precision of 0.25°): one for measuring the excitation displacement x and one for the cart movement y. A force sensor is also employed to monitor the SMA spring force. A power supply is coupled to the ends of the SMA spring to promote heating by the Joule effect. Because system response is highly temperature dependent, changes in electrical current induce different system behaviours. The pretension level of the SMA spring is defined by the length of the thread between the cart and the linear spring. Geometric properties of the SMA spring, the properties of the system components, and characteristic quantities of the system are shown in table 1.

The SMA helical spring is manufactured from an SMA wire with the aid of a device that defines the shape and clamps the spring ends. Afterwards, it is necessary to promote a heat treatment that induces recrystallization, defining the spring form as the natural one. This treatment depends on the size of the spring. Here a Ni-Ti wire is employed and the heat treatment is done by heating the spring to 500 °C for 30 minutes and, after that, cooling it in a water medium.

The SMA temperature is not directly measured. Because there is a direct relation between electrical power and the temperature of SMA wires Furst and Seelecke 2012, electric current is used to evaluate temperature. It is known that the electrical resistances are different for austenite and martensite. Here we are interested in constant temperature conditions, represented by constant applied electrical current. Due to the resistance changes associated with phase transformations, the electrical power also changes. Therefore, there are temperature fluctuations. However these temperature fluctuations are considered to be small and are therefore ignored. In the analysis presented in this paper, an almost (but not completely) linear relationship between electrical current and temperature is assumed due to changing resistance. Most of the measurements in this work are performed only either at room temperature or under such hot conditions that the SMA spring consists of pure austenite. The minimum and maximum values are stated in table 1.

3. Theoretical modelling

The modelling of the dynamic system is split into three parts: (a) the one-dimensional Brinson model for describing the pseudoelastic shape memory alloy; (b) modelling of a helical spring; (c) equations of motions for the dynamic system. Two modifications to the Brinson model are proposed to get better resemblance with experiments.

3.1. Constitutive equations—Brinson's model

The constitutive model by Brinson Brinson 1993, Brinson and Huang 1996, Bekker and Brinson 1998 describes the one-dimensional tensile behaviour of shape memory alloys. Here we are interested in pseudoelastic behaviour, and therefore, the original model is simplified, neglecting twinned

martensite. Twinned martensite is formed only when the temperature is below the martensitic start temperature M_s, which is below the lowest operational temperature (i.e., room temperature) for the current material; cf table 3. The stress state in the spring loaded by axial force is pure shear for small deflection (Budynas *et al* 2008). Although the Brinson model was originally proposed to describe tension-compression behaviour, SMAs have qualitatively similar characteristics in shear, and therefore the model can be employed for this aim. Hence, converting the model for high-temperature shear representation, the following constitutive equation describes the SMA behaviour.

$$\tau = G\left(\gamma - \gamma_L \xi\right), \tag{1}$$

where τ is the shear stress, γ is the shear strain, and ξ is the martensitic volume fraction. Note that in the original Brinson model $\xi = \xi_T + \xi_S$ represents both twinned and detwinned martensite. Here, because the description is restricted to high-temperature behaviour, ξ is the volume fraction of detwinned martensite, i.e., $\xi_T = 0$.

Besides, $G = G_A + \xi\,(G_M - G_A)$, where G_M and G_A are the shear moduli of martensite and austenite respectively, and γ_L is the residual shear strain caused by phase transformation. Note that the usual thermoelastic expansion term is neglected in equation (1) because its influence is at least an order of magnitude lower than the effects from the phase transformations. Moreover, this model does not take into account temperature changes in the material due to mechanical deformation as well as the exo- and endothermic properties of the phase transformations. Other models that are rate-dependent do take this into account, e.g., Lagoudas *et al* (2012), Monteiro *et al* (2009).

The volume fraction of detwinned martensite evolution is defined as a function of temperature T and stress τ. In this regard, the forward transformation (from austenite to detwinned martensite) is given by:

- If $\dot{\tau} - C_A\dot{T} > 0$ and $\tau_{ms} \leqslant \tau \leqslant \tau_{mf}$ then

$$f_M(\tau, T) = \frac{1}{2} - \frac{1}{2}\cos\left(\pi\frac{\tau - \tau_{ms}}{\tau_{mf} - \tau_{ms}}\right) \tag{2}$$

$$\xi = \xi_0 + \left(1 - \xi_0\right)f_M(\tau, T) \tag{3}$$

The reverse transformation (from detwinned martensite to austenite) is described by:

- If $\dot{\tau} - C_M\dot{T} < 0$ and $\tau_{af} \leqslant \tau \leqslant \tau_{as}$ then

$$f_A(\tau, T) = \frac{1}{2} - \frac{1}{2}\cos\left(\pi\frac{\tau - \tau_{af}}{\tau_{as} - \tau_{af}}\right) \tag{4}$$

$$\xi = \xi_0 f_A(\tau, T) \tag{5}$$

- Otherwise, $\dot{\xi} = 0$.
- Furthermore, $\xi = 1$ if $\tau > \tau_{mf}$, and $\xi = 0$ if $\tau < \tau_{af}$.

The boundaries in the simplified stress-temperature phase diagram are

$$\begin{aligned} \tau_{ms} &= C_M\left(T - M_s\right), \quad \tau_{mf} = C_M\left(T - M_f\right) \\ \tau_{as} &= C_A\left(T - A_s\right), \quad \tau_{af} = C_A\left(T - A_f\right). \end{aligned} \tag{6}$$

The temperatures M_s and M_f are the start and finish transformation temperatures for the forward transformation, and A_s and A_f are the austenitic counterparts. These temperatures refer to a stress-free state. Furthermore, C_A and C_M denote the slopes of the austenite and martensite formation boundaries in the temperature-stress phase diagram.

It should be observed that ξ also depends on the constant ξ_0 that represents the value of ξ at the start of phase transformation. Note that ξ_0 is associated with previous phase transformations that occurred during load history. The value of ξ_0 changes whenever either $\dot{\tau} - C_A\dot{T}$ or $\dot{\tau} - C_M\dot{T}$ changes sign. A far more thorough explanation is given by Bekker and Brinson (1998).

The functions for f_M and f_A, equations (2) and (4), are hardening functions, and the functions for ξ, equations (3) and (5), control the sub-loop behaviour. For both of these types of functions, modifications are proposed in the next section.

This model is constructed in such a way that γ can be found explicitly as a function of τ and T, because ξ is an explicit function of τ and T. However, when using such models in dynamic problems, the inverse problem is usually of interest. Hence, it is important to evaluate stress τ as a function of deformation γ. This means that iterative procedures have to be used, and it is suggested to use a Newton-Raphson iteration procedure between steps in strain. This requires the use of the derivatives of strain $\gamma(\tau, T)$ with respect both to stress and temperature (keeping the other variable constant). They are easily found by differentiation of the governing equation (1):

$$\frac{\partial\gamma}{\partial\tau} = \frac{1}{G} + \left(\frac{G_A - G_M}{G^2}\tau + \gamma_L\right)\frac{\partial\xi}{\partial\tau}, \tag{7}$$

$$\frac{\partial\gamma}{\partial T} = \left(\frac{G_A - G_M}{G^2}\tau + \gamma_L\right)\frac{\partial\xi}{\partial T}. \tag{8}$$

The differentials $\frac{\partial\xi}{\partial\tau}$ and $\frac{\partial\xi}{\partial T}$ are piecewise functions, found by differentiation of the hardening functions and sub-loop functions equations (2)-(5).

3.2. Modified hardening and sub-loop functions

The cosine hardening functions f_A and f_M are smooth because of their differentiability in addition to continuity and also because of their horizontal tangents at the boundaries. Horizontal tangents are necessary to get smooth transitions between the thermoelastic regions and phase transformation regions. However, the level of smoothness cannot be controlled. When comparing with experiments, greater similarities can be achieved by using other smooth functions, where the smoothness at each boundary can be controlled

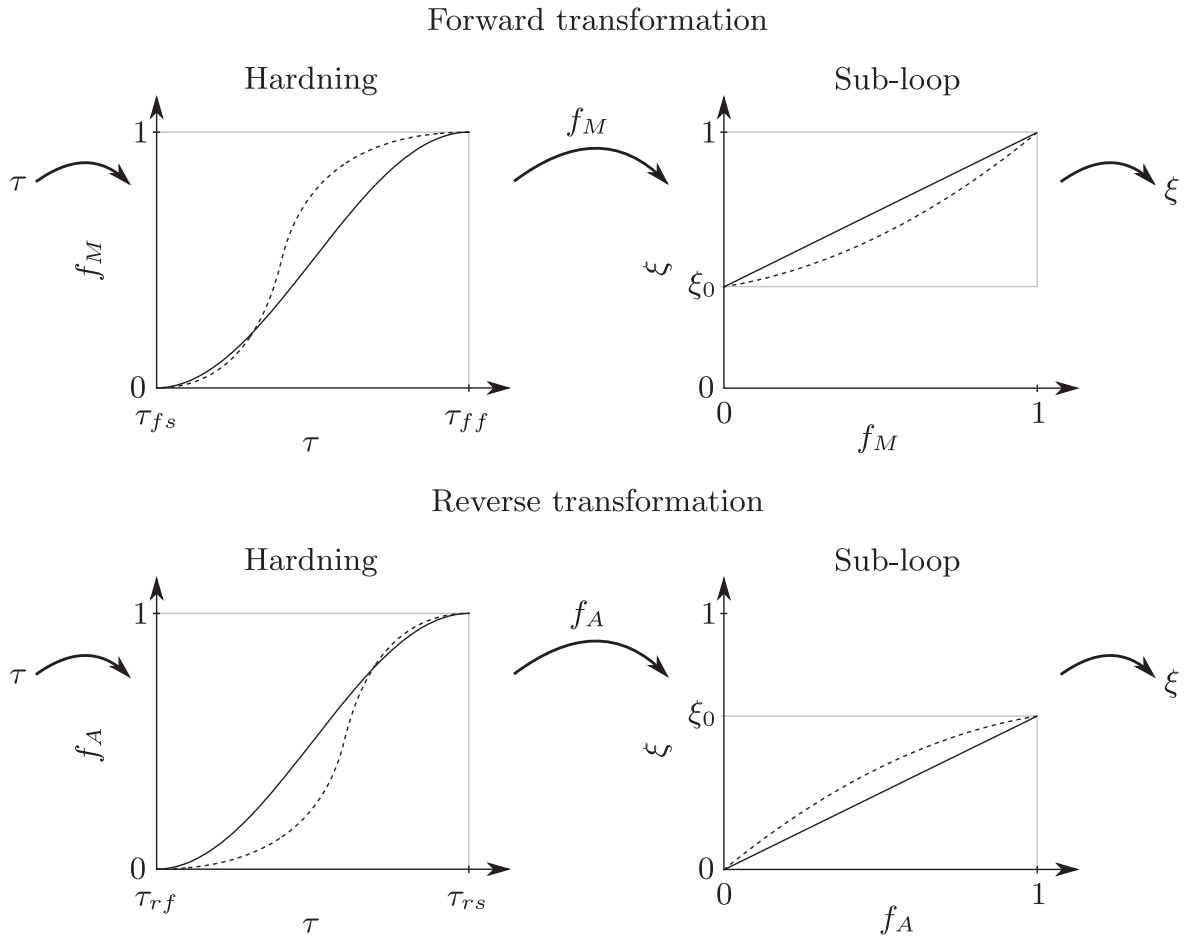

Figure 2. Hardening and sub-loop functions in the forward and reverse transformations. The stress (τ) is input to the hardening function, whose output (f_M or f_A) is input to the sub-loop function, whose output is ξ. The solid lines are the cosine hardening function and the linear sub-loop functions as in the Brinson model. The dashed lines are examples of the proposed smooth hardening functions and cubic sub-loop functions.

individually. Initially Liang and Rogers (1990) proposed to use cosine functions for describing the hardening kinetics, and later the functions were adapted by Brinson (1993). The choice of a cosine hardening function was empirically based, and therefore other types of functions are equally valid. A novel smooth hardening function is presented, and it is inspired by a smooth hardening function presented by Lagoudas *et al* (2012).

Due to the complex shear stress-strain distributions in the helical springs, the Brinson model does not reproduce all aspects of the thermo-mechanical behaviour of the springs. An alteration of sub-loop functions, which initially are linear functions in f_A or f_M respectively, provides a better resemblance with experimental data. This means that the proposed alternative sub-loop functions counteract the consequence of the simple model and its assumptions for the mechanical model of the helical spring used in this paper. An illustration of the existing and proposed hardening and sub-loop functions is shown in figure 2.

3.2.1. Hardening function. The proposed function consists of two successive quadratic Bézier curves $\mathbf{B}^i(s)=(\mathbf{B}^i_x(s), \mathbf{B}^i_y(s))$ for $i = 1, 2$, which replaces the existing function $f(x) = \frac{1}{2} - \frac{1}{2}\cos(\pi x)$ for $x \in [0; 1]$ (equations (2) and (4)).

The choice of Bézier curves is taken because it is easy to control smoothness. Two successive quadratic curves are chosen instead of a single cubic curve because of simpler mathematical expressions. A minor advantage of the cubic curve is that it is infinitely differentiable (C^∞), whereas the two successive quadratic curves are only able to ensure one-time differentiability in addition to continuity (C^1). The Bézier curves are used to shape the hardening function:

$$f(x) = \begin{cases} \left\{ \mathbf{B}^1_y(s) \;\middle|\; \mathbf{B}^1_x(s) = x \right\} & \text{for} \quad 0 \leqslant x \leqslant a \\ \left\{ \mathbf{B}^2_y(s) \;\middle|\; \mathbf{B}^2_x(s) = x \right\} & \text{for} \quad a < x \leqslant 1 \end{cases} \tag{9}$$

The first curve $\mathbf{B}^1(s)$ is defined by the three points (0, 0), (n_1, 0), and (a, b). The second curve $\mathbf{B}^2(s)$ is defined by the three points (1, 1), (1 − n_2, 1), and (a, b). This means that the curves start at the boundaries for $s = 0$ and meet for $s = 1$. The two curves are oriented oppositely to get simpler mathematical expressions. The result is the same. The point (a, b) is determined such that $(\mathrm{d}\mathbf{B}^1/\mathrm{d}s)|_{s=1} = -(\mathrm{d}\mathbf{B}^2/\mathrm{d}s)|_{s=1}$, which ensures one-time differentiability.

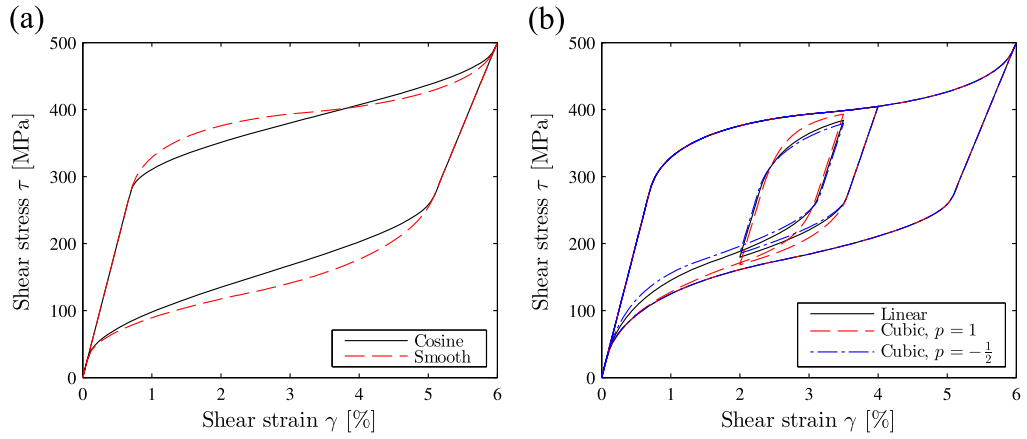

Figure 3. Differences in the stress–strain behaviour between the original and the proposed hardening and sub-loop functions. Hardening functions. (a): for the smooth function, the choice of parameters is $n_1^f = 0.45$ (forward start), $n_2^f = 0.35$ (forward end), $n_1^r = 0.2$ (reverse end), $n_2^r = 0.4$ (reverse start). Subloop functions. (b): for $p > 0$ the hysteresis area increases compared with the linear case; for $p < 0$ it decreases.

The smoothness is controlled by the two non-negative parameters n_1 and n_2, which have to fulfil $0 \leqslant n_1 + n_2 \leqslant 1$. The expressions for the Bézier curves become:

$$\mathbf{B}^1(s) = \begin{Bmatrix} (a - 2n_1)s^2 + 2n_1 s \\ \frac{1}{2}s^2 \end{Bmatrix},$$
$$\mathbf{B}^2(s) = \begin{Bmatrix} (a + 2n_2 - 1)s^2 - 2n_2 s + 1 \\ -\frac{1}{2}s^2 + 1 \end{Bmatrix}, \quad (10)$$

where $a = \frac{1}{2}(n_1 - n_2 + 1)$. The variable s is substituted such that the first coordinate x becomes the independent variable and the second coordinate y becomes the dependent variable. The final expression for the hardening function is as follows:

$$f(x) = \begin{cases} \frac{1}{2}s^2 \quad \text{where } s = \dfrac{-n_1 + \sqrt{n_1^2 + (a - 2n_1)x}}{a - 2n_1} & \text{for } 0 \leqslant x \leqslant a \\ 1 - \frac{1}{2}s^2 \quad \text{where} & \\ \quad s = \dfrac{n_2 - \sqrt{n_2^2 - \left(a + 2n_2 - 1\right)(1 - x)}}{a + 2n_2 - 1} & \text{for } a < x \leqslant 1 \end{cases} \quad (11)$$

Special cases exist for s if $a - 2n_1 = 0 \wedge 0 \leqslant x \leqslant a$ and $a + 2n_2 - 1 = 0 \wedge a < x \leqslant 1$ because of singularities in equation (11). In these cases, $s = \frac{x}{2n_1}$ and $s = \frac{1-x}{2n_2}$ respectively from equation (10).

It is suggested that different sets of smoothing parameters (n_1, n_2) be used for the forward and reverse transformations. For this reason, the smoothing parameters for the forward transformation are denoted (n_1^f, n_2^f), and for the reverse transformation they are denoted (n_1^r, n_2^r).

An example of the smooth hardening function is seen in figure 3(a), where it is compared with the existing cosine hardening function.

3.3. Sub-loop function

A sub-loop function is proposed in order to alter the height and thereby the average stiffness and the enclosed area of the sub-loops. The area of the sub-loops determines the dissipation characteristics. Therefore, the linear sub-loop functions (equations (3) and (5)) are replaced by cubic counterparts that have to fulfil certain conditions in order to get reasonable behaviour.

For the forward transformation, the original sub-loop function is $g_0(x) = \xi_0 + (1 - \xi_0)x$ for $x \in [0; 1]$. The proposed sub-loop function g has the same boundary values: $g(0) = \xi_0$ and $g(1) = 1$. Furthermore, it is monotone and fulfils $g(x)|_{\xi_0^a} < g(x)|_{\xi_0^b}$ for any $\xi_0^a < \xi_0^b$ and any $x \in [0; 1]$. A cubic function satisfying this is

$$g(x) = \xi_0 + \left(1 - \xi_0\right)x - px(1 - x)q(x), \quad (12)$$

where $q(x)$ is a piecewise function in ξ_0:

$$q(x) = \begin{cases} \xi_0(2 - x) & \text{for} \quad 0 \leqslant \xi_0 \leqslant \frac{1}{3} \\ \left(1 - \xi_0\right)(1 - x) + \xi_0 x & \text{for} \quad \frac{1}{3} < \xi_0 \leqslant \frac{2}{3} \\ \left(1 - \xi_0\right)(1 + x) & \text{for} \quad \frac{2}{3} < \xi_0 \leqslant 1\ . \end{cases} \quad (13)$$

The parameter $p \in \left[-\frac{1}{2}; 1\right]$ controls the sub-loop characteristics.

For the reverse transformation, a cubic function that satisfies similar requirements is:

$$h(x) = \xi_0 x + px(1 - x)q(x)\ . \quad (14)$$

Note that both $g(x)$ and $h(x)$ are equal to the linear sub-loop functions for the parameter $p = 0$. It is suggested to use the same value of p for both forward and reverse transformation. An example of the effect of changing the sub-loop functions is seen in figure 3(b). By using $p < 0$ the average stiffness and the sub-loop area decrease. For $p > 0$ the stiffness and area increase. In this regard, an increase is wanted in order to

Table 2. Properties for dissipation due to friction and viscous damping used for numerical simulation.

μ	c	g	d
2.1×10^{-3}	10^3 s m^{-1}	9.81 N kg^{-1}	0.11 N s m^{-1}

get better resemblance with experiments. As seen later, p has been chosen to be equal to unity.

3.4. Helical spring model

Aguiar *et al* (2010) discussed the modelling of SMA helical springs, showing that it is sufficient to assume a linear shear strain distribution and a constant phase transformation in the wire cross section. The relation between the elongation of the spring y and the shear strain in the periphery γ_r is

$$\gamma_r = \frac{r}{2\pi NR^2} y \,. \tag{15}$$

Here r is the wire radius, N the number of coils, and R the radius of the spring. The strain distribution is linear, $\gamma = \frac{a}{r}\gamma_r$ for $a \in [0; r]$. The relation between the spring force F and the shear stress τ is

$$F = \frac{2\pi}{R} \int_0^r \tau(a)\, a^2 \mathrm{d}a \tag{16}$$

Because τ is a nonlinear function in γ, this integral cannot be solved directly. Nevertheless, it is possible to obtain good results by assuming that $\xi = \tilde{\xi}$ is constant throughout the cross section, which combined with the governing equation (1) yields

$$F = \frac{2\pi}{R} \int_0^r G\left(\frac{a}{r}\gamma_r - \gamma_L \tilde{\xi}\right) a^2 \mathrm{d}a = \frac{2\pi r^3}{3R} G\left(\tfrac{3}{4}\gamma_r - \gamma_L \tilde{\xi}\right) \tag{17}$$

Moreover, an equivalent constant strain $\tilde{\gamma} = \frac{3}{4}\gamma_r$ is chosen such that an equivalent constant stress $\tilde{\tau} = G(\tilde{\gamma} - \gamma_L \tilde{\xi})$ fulfils the governing equation and

$$F = \frac{2\pi r^3}{3R} \tilde{\tau} \,. \tag{18}$$

Substituting $\tilde{\gamma}$ into equation (15), it becomes

$$\tilde{\gamma} = \frac{3r}{8\pi NR^2} y \,. \tag{19}$$

By using equations (18) and (19) together with the governing equation (1), the relation between elongation y and spring force F can be found.

3.5. Equation of motion and its solution

The equation of motion for the cart is obtained by Newton's Second Law (see figure 1(b)):

$$m\ddot{y} = -F_p(y, T, \xi_0) + F_f(\dot{y}) + F_e(x, y), \tag{20}$$

The linear spring force is $F_e = k_l(x - y + x_0)$, where k_l is the linear spring stiffness and x_0 is a length measure of constant pretension. This means that the pretension x_0 is not related to the stiffness and length of the PE spring but to the linear spring. The excitation x is either zero (for free vibrations) or sinusoidal (forced vibrations): $x(t) = A \sin(2\pi\omega t + \phi)$. The system dissipation, different from hysteretic behaviour, can be described by $F_f(\dot{y}) = -\mu mg\frac{2}{\pi}\arctan(c\dot{y}) - d\dot{y}$, where c is a numerically aiding constant and g is the gravitational constant. This is a continuous approximation to dynamic Coulomb friction, with friction coefficient μ combined with viscous damping with the damping factor d. The chosen values used for describing these dissipative effects are seen table 2. The PE spring force $F_p(y)$ is determined as described in the preceding sections (in which it is denoted F).

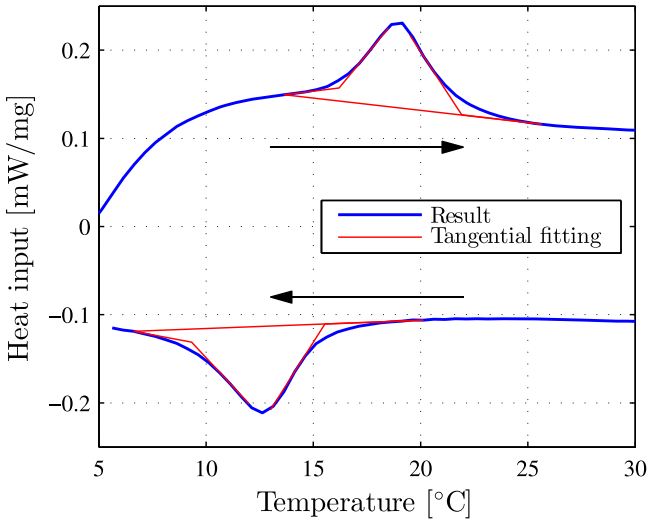

Figure 4. The resulting graph from a DSC test. The red lines indicate the method of determining the transformation temperatures.

Table 3. Transformation temperatures for the PE spring extracted from the DSC test.

A_s	A_f	M_s	M_f
16.2 °C	21.9 °C	15.5 °C	9.3 °C

3.5.1. Standard approach for numerical solution. The Runge-Kutta-Fehlberg method is used to solve the equation of motion (20) in a state space formulation by defining a second state $z \equiv \dot{y}$. At each time step, the vector (y, z) is supplied and the derivatives are found:

$$F_p = F_p(y, T, \xi_0) \qquad \text{(inverse problem)} \tag{21}$$

$$\dot{y} = z \tag{22}$$

$$\dot{z} = \frac{1}{m}\left(-F_p - \mu mg\frac{2}{\pi}\arctan(cz) - dz + k_l(x - y + x_0)\right). \tag{23}$$

As mentioned in section 3.1, the PE force F_p has to be found by iterative procedures.

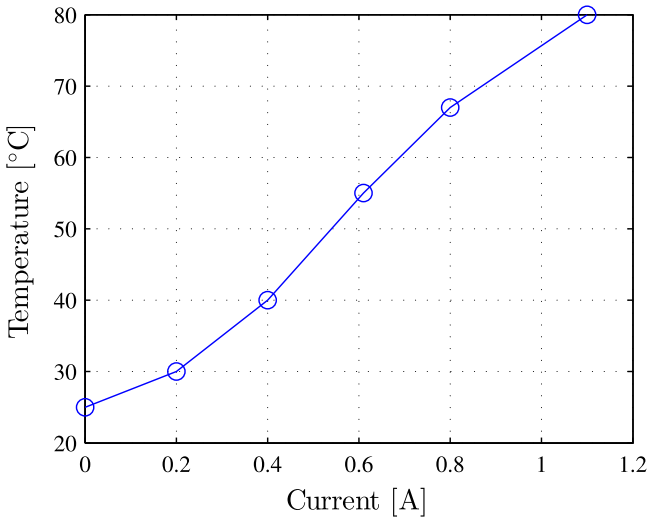

Figure 5. Relationship between electrical current through the PE spring and the assumed temperature.

3.5.2. Particular approach for numerical solution. The iterative procedure of the Brinson model can be avoided by changing the state variables so that the displacement y is found from F_p instead, because it is an explicit function. The displacement is substituted with the PE force as a state variable, which means that each time step $\left(F_p, z\right)$ is supplied and the derivatives are determined:

$$y = y\left(F_p, T, \xi_0\right) \qquad \text{(explicit relation)} \tag{24}$$

$$\dot{F}_p = \left(\frac{\partial\tilde{\gamma}}{\partial\tilde{\tau}}\frac{\partial\tilde{\tau}}{\partial F_p}\right)^{-1} \times \left[z\left(\frac{\partial y}{\partial\tilde{\gamma}}\right)^{-1} - \dot{T}\frac{\partial\tilde{\gamma}}{\partial T}\right] \quad \text{(explicit relation)} \tag{25}$$

$$\dot{z} = \frac{1}{m}\left(-F_p - \mu m g\frac{2}{\pi}\arctan\left(cz\right) - dz + k_l(x - y + x_0)\right). \tag{26}$$

The expression for $\dot{F}_p$ is found from the velocity:

$$z = \frac{\mathrm{d}y}{\mathrm{d}t} = \frac{\partial y}{\partial\tilde{\gamma}}\left(\frac{\partial\tilde{\gamma}}{\partial\tilde{\tau}}\frac{\partial\tilde{\tau}}{\partial F_p}\frac{\mathrm{d}F_p}{\mathrm{d}t} + \frac{\partial\tilde{\gamma}}{\partial T}\frac{\mathrm{d}T}{\mathrm{d}t}\right) = \frac{\partial y}{\partial\tilde{\gamma}}\left(\frac{\partial\tilde{\gamma}}{\partial\tilde{\tau}}\frac{\partial\tilde{\tau}}{\partial F_p}\dot{F}_p + \frac{\partial\tilde{\gamma}}{\partial T}\dot{T}\right), \tag{27}$$

where $\frac{\partial\tilde{\gamma}}{\partial\tilde{\tau}}$, $\frac{\partial\tilde{\gamma}}{\partial T}$, $\frac{\partial\tilde{\tau}}{\partial F_p}$, and $\frac{\partial y}{\partial\tilde{\gamma}}$ are found from equations (7), (8), (18), and (19) respectively. These state equations are solved using the Runge-Kutta-Fehlberg algorithm.

This particular approach makes inner iterations of the Brinson model unnecessary, which leads to less numerical computation. Note that $\frac{\partial\tilde{\gamma}}{\partial\tilde{\tau}}$ and $\frac{\partial\tilde{\gamma}}{\partial T}$ also have to be calculated when performing inner iterations. Simulations have shown that this approach saves approximately 10% of the overall computation time.

4. Characterization of pseudoelastic spring

This section presents the characterisation of the PE spring used in the experimental setup. This is done by using a DSC test and also by considering force-displacement curves. Figure 4 and table 3 present results of the DSC test, showing the amount of heat necessary to maintain a constant temperature rate (positive or negative) of a specimen of the SMA. At a peak or valley, phase transformations happen. Note that at room temperature (≈25 °C), the PE spring is stable at the austenitic state because A_f is lower than room temperature. The transformation temperatures are determined by the intersection between the tangent at the absolute highest slope and the tangent at the start or end of the transformation area. This is indicated in figure 4 by the red lines.

The force-displacement experimental test of the PE spring is done by uncoupling the oscillator and the linear spring from the cart in the system shown in figure 1(b), and a chosen displacement path is induced to the cart. Experimental tests are done at different temperatures by inducing distinct (and constant) values of electric current. It is estimated that the temperature is 80 °C when applying 1.1 A. Moreover, a linear relationship between current and the temperature relative to room temperature is initially assumed. Small discrepancies from this linear model are used in order to get slightly better resemblance between the model and the experiments for the overall temperature range. The assumed current-temperature relation is shown in figure 5. This is consistent with the considerations in section 2.

Results of the force-displacement tests and the model fit are shown in figure 6. The model parameters have been determined by nonlinear least square regression of the model prediction to the experimental results. There is a very good resemblance. Only at high temperatures is the model unable to match the experimental curve. This will be reflected in the comparisons throughout this paper. The model parameters used, which are the same for all temperatures, are shown in table 4.

Figure 7 presents a comparison between experimental data with Brinson's model with different hardening and sub-loop functions. Tests are performed at 25 °C. Note that the outer loop is matched very well in all three cases. For the original Brinson model, figure 7(a), there is a small linear region at the beginning of the reverse transformation that is not seen in experiment. Moreover, to get good resemblance at the outer loop the residual strain γ_L has be given a high value (4.99%) so that the cosine hardening behaviour does not interfere at that point. This is again determined by a least square regression scheme that minimized the difference between model predictions and experimental results. On the other hand, this means that the sub-loop behaviour is not captured well. When smooth hardening is introduced (figure 7(b)), the outer loop becomes smoother and the residual strain is reduced to 3.11%, which results in better resemblance in the inner loops. Both average stiffness and hysteresis area of the sub-loops are matched even better when the cubic sub-loop function is also introduced (figure 7(c)).

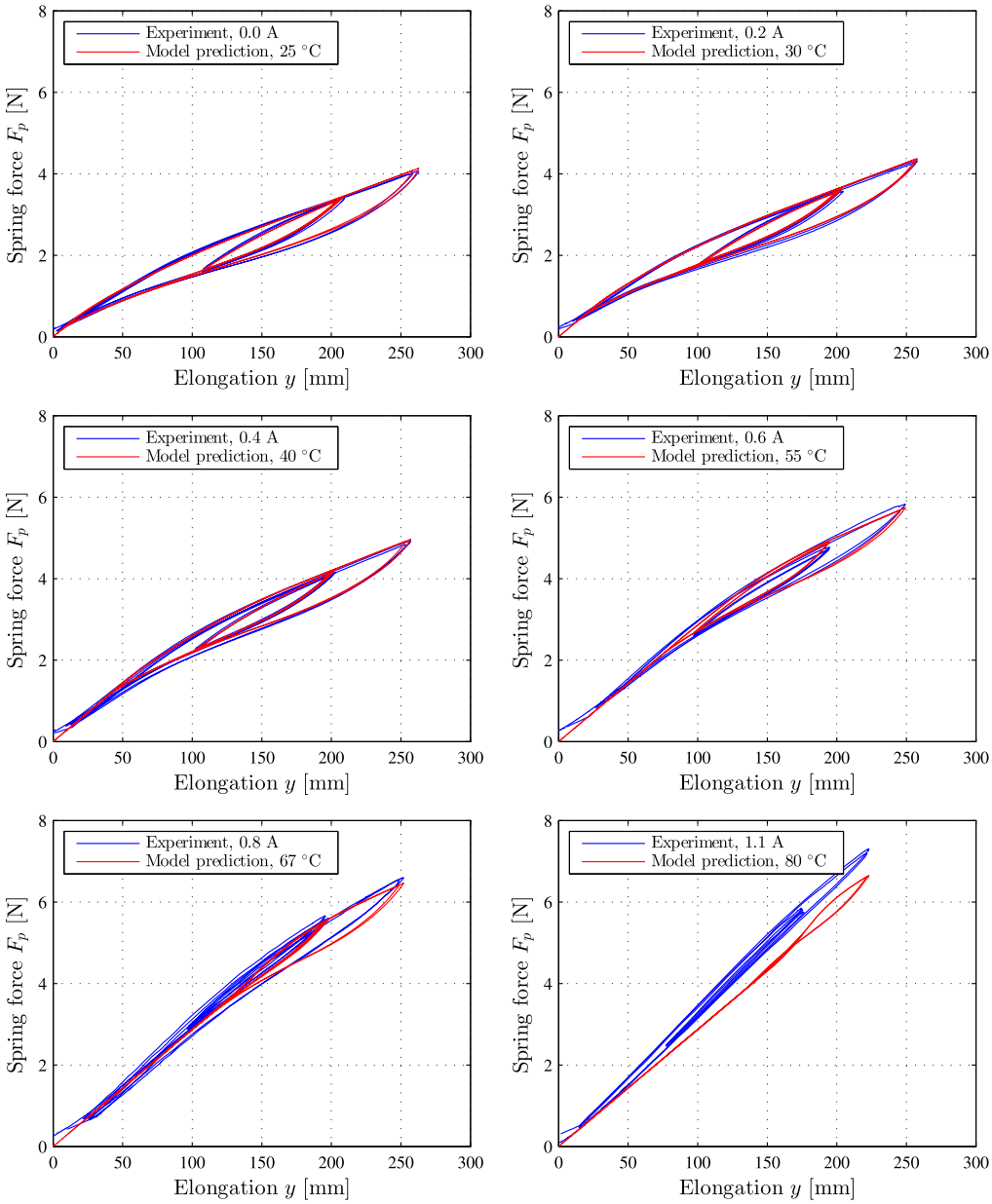

Figure 6. Experimental force–displacement results for the pseudoelastic spring compared with the Brinson model with smooth hardening and cubic sub-loop. The relationship between electrical current and temperature is estimated.

Table 4. Parameters used in the spring model using the Brinson model with smooth hardening and cubic sub-loop.

γ_L	G_A	G_M	A_s	A_f	M_s	M_f
3.11%	16.8 GPa	47.6 GPa	−39.1 °C	22.9 °C	20.0 °C	−32.3 °C
C_A	C_M	n_1^f	n_2^f	n_1^r	n_2^r	p
5.55 MPa °C^{-1}	6.18 MPa °C^{-1}	0.286	0.001	0.166	0.280	1.00

It is important to highlight that the PE spring is subjected to large deformations, reaching more than four times the original length. Therefore, complex stress distributions can be induced, causing non-homogeneous phase transformations (Phillips and Costello 1972, Mirzaeifar *et al* 2011, Lagoudas *et al* 2012). At the spring wire cross section centre, the stress is always (close to) zero, even though the spring is highly loaded globally (Aguiar *et al* 2010). This means that martensite is not induced by stress (i.e., detwinned martensite) at the cross section centre, and therefore the spring material

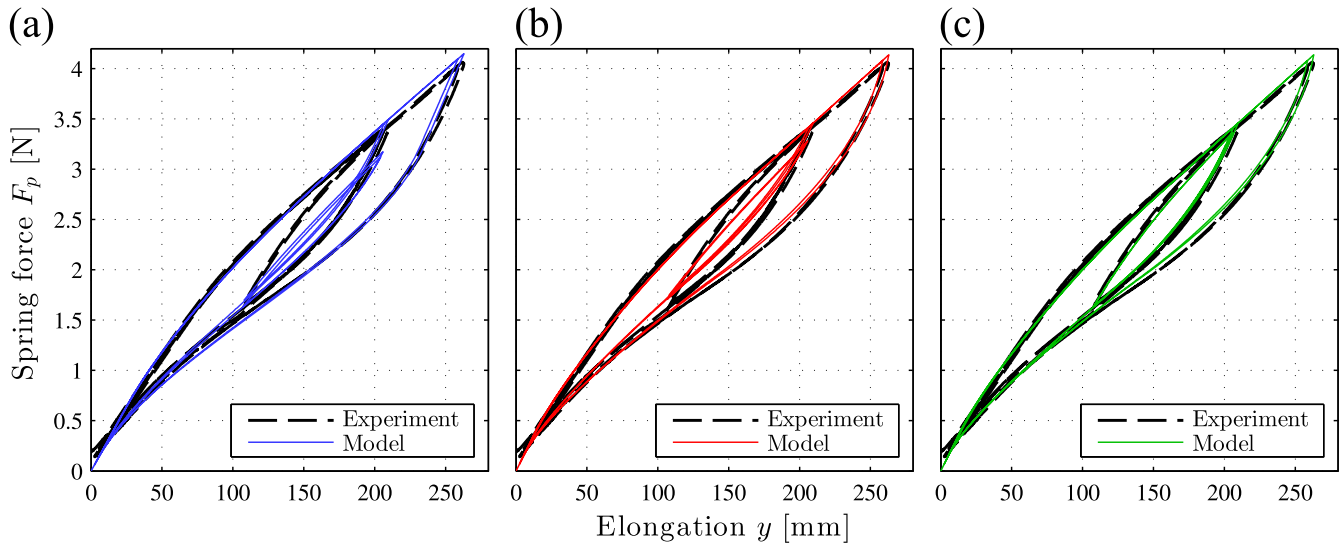

Figure 7. Best fit of the Brinson model with and without modifications to the experimental force–displacement test at 25 °C. (a) Cosine hardening and linear sub-loop; (b) Bézier hardening and linear sub-loop; (c) Bézier hardening and cubic sub-loop.

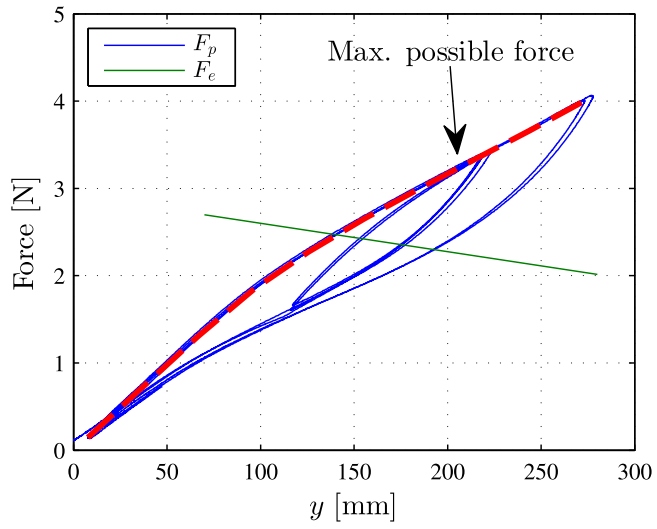

Figure 8. Illustration of the range of equilibrium positions for the dynamic system. The level of pre-tension here is $x_0 = 900$ mm (equivalent to $y_0 = 2.3l_0$ in the sense of $k_0 y_0 = k_l x_0$). For a given position y the PE spring contains the minimum possible amount of martensite at the topmost loading branch in the force–displacement diagram, indicated by the red dashed line.

cannot reach a complete detwinned martensitic state throughout the wire cross section. For the same reason, and because the spring model uses an assumption of constant material properties in the wire cross section, the chosen phase transformation temperatures in the model are not the same as found by the DSC. Furthermore, the model is restricted to displacements below approximately 300 mm ($4.6l_0$) and temperatures from 23 °C to 80 °C because of the choice of parameters.

Inspection of the force-displacement behaviour at room temperature reveals that the initial stiffness at room temperature ($k_0 = 20$ N m^{-1}) is lower than the tangential stiffness of the mixture ($\approx$31 N m^{-1} = $1.6k_0$). This is also reflected in the material parameters, where $G_M > G_A$ (table 4). It is well known that the stiffness of martensite is lower than the stiffness of austenite, but these results show the opposite. This incongruence is believed to be caused by large deformations. For large strains in the spring, normal stresses may be induced, resulting in a stiffening effect (Phillips and Costello 1972, Mirzaeifar *et al* 2011, Lagoudas *et al* 2012). This means that the apparent martensitic stiffness is higher than the actual martensitic stiffness. The stiffening effect due to the geometry is also the reason why the stiffness in the high-temperature condition is higher in experiment (34 N m^{-1} = $1.7k_0$) than in model prediction (29 N m^{-1} = $1.4k_0$). The geometric stiffening effect is not incorporated in the model. During transformation, the stiffness is lower (10 N m^{-1} = $0.5k_0$) than the initial stiffness. This means that the stiffness changes up to a factor of three (10 N m^{-1} to 34 N m^{-1}) between different conditions of stress and temperature; cf figure 6.

The dissipation due to hysteresis is an important characteristic of the PE spring. Note that the increase of displacement tends to be related to the increase of dissipation due to the larger hysteresis loops. Furthermore, for increasing temperature, the hysteresis loops are smaller, indicating less dissipative capabilities. The average stiffness and the hysteresis are coupled properties.

5. Free vibrations

The free vibration analysis considers the setup shown in figure 1(a) by implying that the DC motor is turned off. Temperature influence is investigated during the tests, considering two cases: constant and varying temperatures.

An equilibrium position is a point in y where the sum of forces acting on the cart vanishes. Therefore, it should be a proper balance between the elastic spring force F_e and the PE

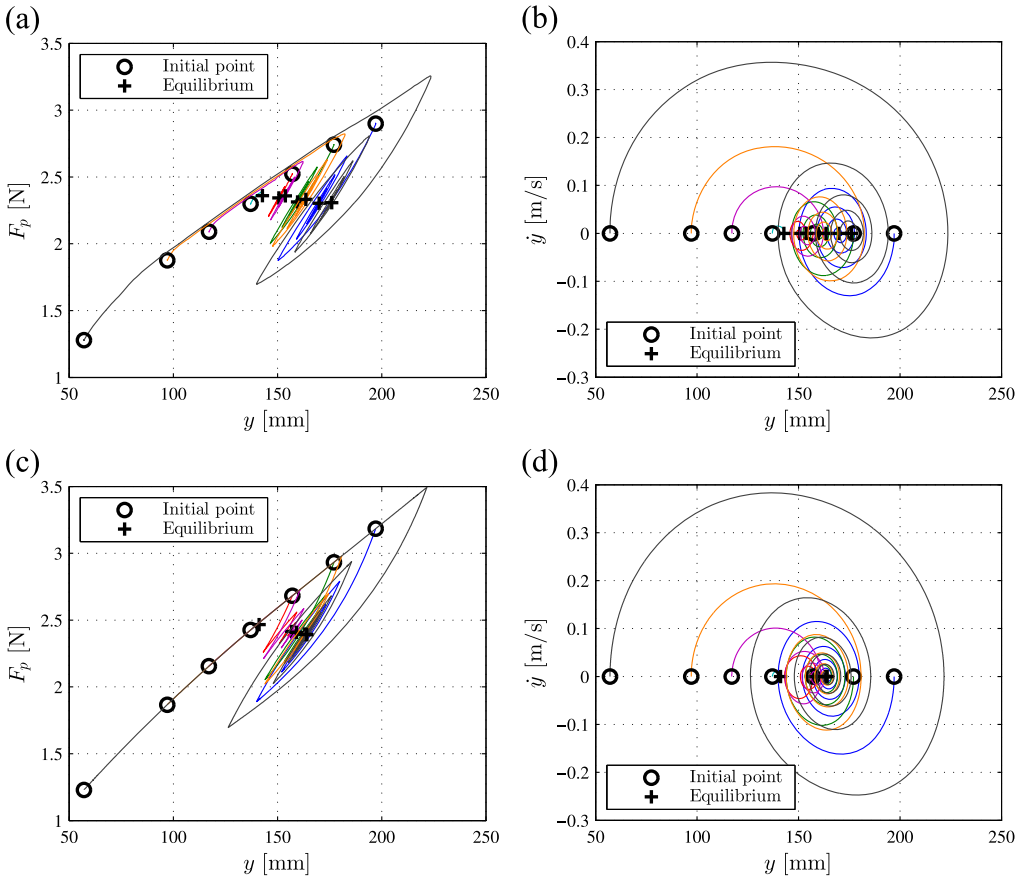

Figure 9. Experimental results (a, b) and numerical simulations (c, d) for force and state space of free vibration with seven different initial conditions indicated by different line colours. The level of pretension is $x_0 \approx 870$ mm ($2.2l_0$) in the experiments but $x_0 = 900$ mm ($2.3l_0$) in the numerical simulations. The specified temperature is $T = 23$ °C in the simulations.

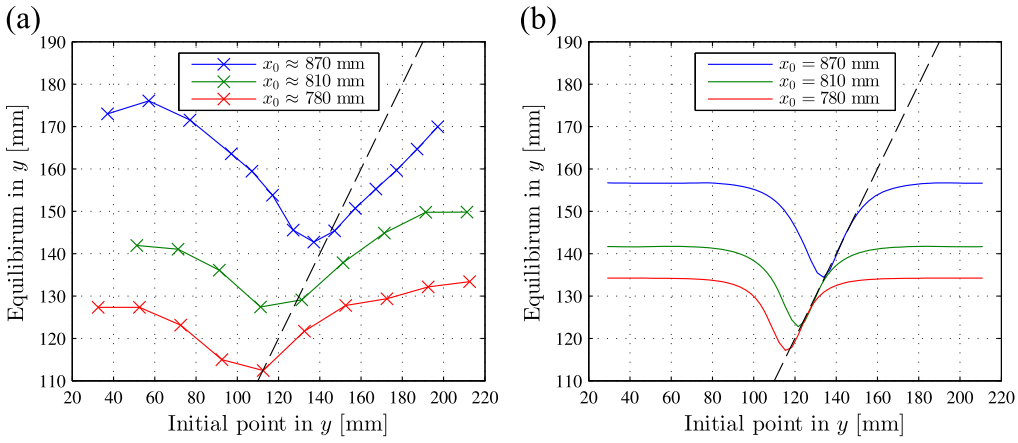

Figure 10. The equilibrium changes both as a function of the initial point and the level of pretension. Here it is illustrated both by experiments (a) and by simulation (b) modelling. The dashed black line indicates identical initial position and equilibrium. For the theoretical results $T = 23$ °C is used.

spring force F_p, namely $F_e = F_p$. Figure 8 shows the force-displacement curves for both springs of this system. The intersections between the blue and green lines establish a proper balance between the spring forces, representing equilibrium positions. Note that the lines are crossing four times, but one could imagine an infinite number of possibilities along the green line, which can be called the 'equilibrium line', for values of y larger than approximately 140 mm in this case, because this is the maximum force considered for the PE spring. It should be pointed out that there is only one equilibrium point at any instant in time and cart position, but the equilibrium is able to move along the line. The vertical

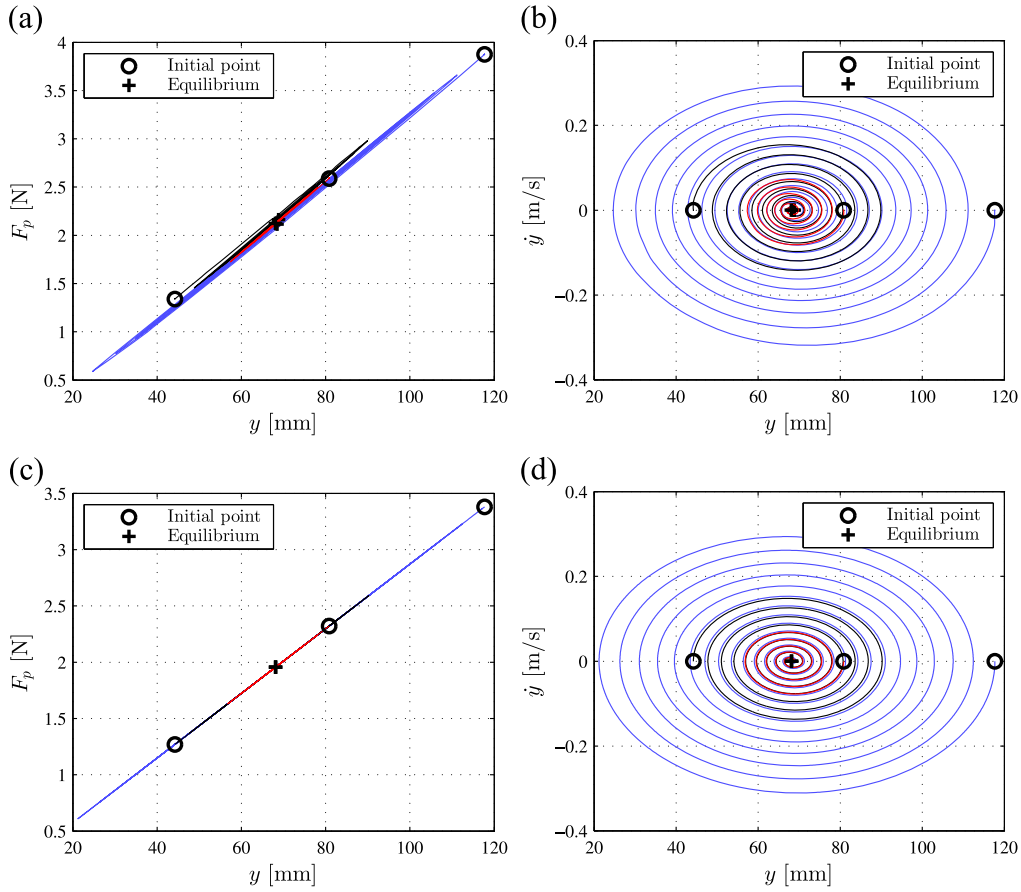

Figure 11. Force and state space for three free vibration tests, both experimentally (a, b) and theoretically (c, d), using different initial positions. In the experiment the PE spring is heated by 1.0 A and the pretension level is approximately 715 mm ($1.8l_0$). The simulation temperature is $T = 80$ °C, and the level of pretension is $x_0 = 670$ mm ($1.7l_0$).

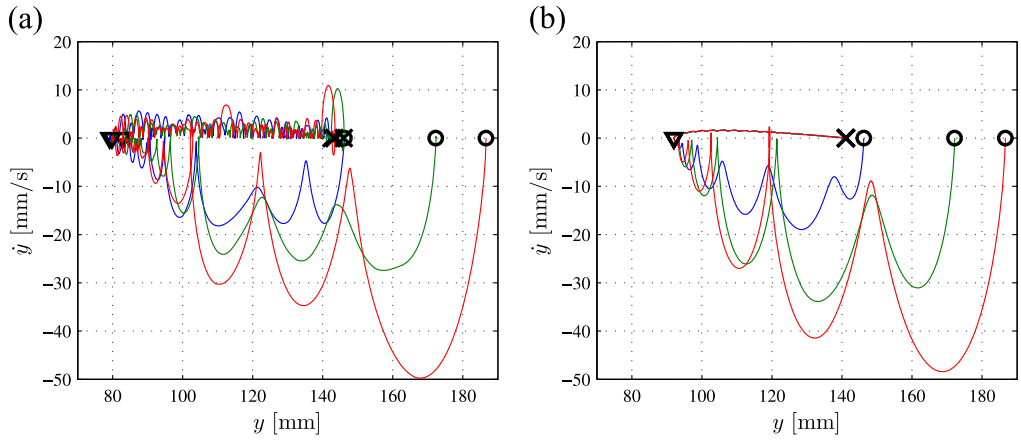

Figure 12. Experimentally obtained (a) and simulated (b) equilibrium position changes due to temperature variations, shown here by three tests (distinct colours) using different initial positions. The initial positions are indicated by ○; during heating of the PE spring, the cart moves to ▽; and it reverses to × during cooling of the spring. In experiments $x_0 \approx 900$ mm ($2.3l_0$), in modelling $x_0 = 905$ mm ($2.3l_0$)

position of the green line is determined by the amount of pretension x_0.

5.1. Constant temperature

Free vibration tests are done by releasing the cart from a range of positions, measuring the displacement and the PE force until the cart is at rest. Both the linear and the PE spring are attached to the cart. At the initial position of each test, it is ensured that the PE spring produce the highest possible force for the given position y, as indicated in figure 8. This is done in order to maintain comparability between the tests.

The first test is done by considering three levels of pretension in room temperature. The pretension level is defined by the length of the thread between the linear spring and the cart, which can be changed. Furthermore, a test is done with the PE spring heated with 1.0 A of electric current.

In figure 9, seven of the tests for a single pretension level at room temperature are shown, highlighting the initial positions (black circles) and their respective resting points/equilibria (black plus signs). The state space plot shows that there is a great amount of energy dissipation due to the hysteresis and other dissipation mechanisms in the system. Experimental tests (figures 9(a) and (b)) are followed by numerical simulations (figures 9(c) and (d)). Generally, there is good agreement with the experimental tests. All qualitative properties are reproduced. However, the stiffness of the PE spring is higher in the simulations. This is probably caused by temperature variations during tests. Thermo-mechanical couplings may drastically affect tests, depending on frequency (Monteiro *et al* 2009), and this is not considered in simulations.

The initial and resting positions for each of the three tests using different pretension levels are highlighted in figure 10. For the three values of pretensions, the starting point is varied in a range of 170 mm ($2.6l_0$), and this gives a variation of 30 mm ($0.5l_0$) to the equilibrium positions in the experimental tests. It is seen that if the starting point is far away from the equilibrium point (long distance from the starting point to the black dashed line), the equilibrium point is almost constant for the two low levels of pretensions. This is also the case for the simulations. Only close to the black dashed line does the equilibrium depend on the starting position. These results show that the equilibrium position depends on the starting position, the initial amount of martensitic phase, and the pretension level. The discrepancies between experimental results and theoretical predictions in figure 10 are the same as for figure 9. Small differences in stiffness and hysteresis between model and experiment have large impact on the resting position.

Experimental and theoretical results of the high-temperature test are shown in figure 11. From the experiments, it is seen that the PE spring force is almost linear, indicating that phase transformations are not occurring, even though the displacements are large. As a consequence, there is a smaller amount of energy dissipation as shown in the state space behaviour. The dissipation is now primarily due to dissipation effects different from hysteretic behaviour, and the level of dissipation is matched very well in the simulations. Due to the linear behaviour of the PE spring, the equilibrium position is almost constant. Furthermore, the equilibrium position has a smaller y-value when compared with the low temperature results because of the higher average PE stiffness ($36\ \mathrm{N\ m^{-1}} = 1.8k_0$). This change due to temperature will be further investigated in the following sections.

5.2. Varying temperature

This section deals with tests where the cart initially rests at one of its equilibrium positions in room temperature, evaluating the influence of temperature changes. The PE spring is heated, causing the cart to move, and then the spring is cooled down by forced convection with the use of an air blower. Again, this causes the cart to move. The test is performed three times with distinct initial conditions without changing the level of pretension. Experimental and numerical results are shown in figure 12. By heating the PE spring in tension, phase transformation to a fully austenitic state takes place. The equilibrium position at this state is independent of the starting point (the ∇ symbols in figure 12). When the spring is cooled down, the cart moves backwards, but only to a minimum amount of detwinned martensite, which is also independent of the starting point. These results show that it is possible to get to the same position, a zero position, no matter what prior activity the spring has been exposed to, simply by heating and cooling the spring, if the heat treatment happens quasi-statically so that inertia effects are low. This zero position lies on the line of maximum possible PE force; cf figure 8. Note that the distance between the equilibrium positions is large compared with the initial length of the spring; see table 1.

The temperature paths induced into the spring in simulation are defined as follows:

$$\text{Heating:}\quad T(t) = 23\ ^\circ\mathrm{C} + (80\ ^\circ\mathrm{C} - 23\ ^\circ\mathrm{C}) \times \left(1 - \exp\left\{-\frac{t}{6.5\ \mathrm{s}}\right\}\right) \tag{28}$$

$$\text{Cooling:}\quad T(t) = 80\ ^\circ\mathrm{C} + (23\ ^\circ\mathrm{C} - 80\ ^\circ\mathrm{C}) \times \left(1 - \exp\left\{-\frac{t}{15\ \mathrm{s}}\right\}\right) \tag{29}$$

For the heating, the spring starts at 23 °C and ends at 80 °C through a first-order low-pass filter with a time constant of 6.5 s. For the cooling, the temperatures are opposite, and the spring changes as through a similar filter with a time constant of 15 s. First-order low-pass filtered temperature changes are related to heating and cooling of a material with constant thermal properties (heat capacity and thermal conductivity) subjected to constant heat and collected radiation and convection being proportional to the temperature relative to room temperature. The filter constants are chosen such that the overall speed matches the experiments. The cooling process is significantly slower than the heating process.

The simulations are in good agreement with the experimental results. The jagging behaviour is captured well. By numerical simulation, it can be shown that this behaviour is solely due to the phase transformations, and it is not caused by other dissipation forces, e.g., the Coulomb friction. Note that the equilibrium positions at the hot state are different in simulation and experiments (y = 92 mm and y = 80 mm respectively). This is because the simulated stiffness of the austenite is lower than the measured stiffness as seen before in figure 6. The difference is therefore expected.

6. Forced vibrations

Forced vibration is now of concern when considering that the system is excited by a DC motor rotating a lever, which pulls

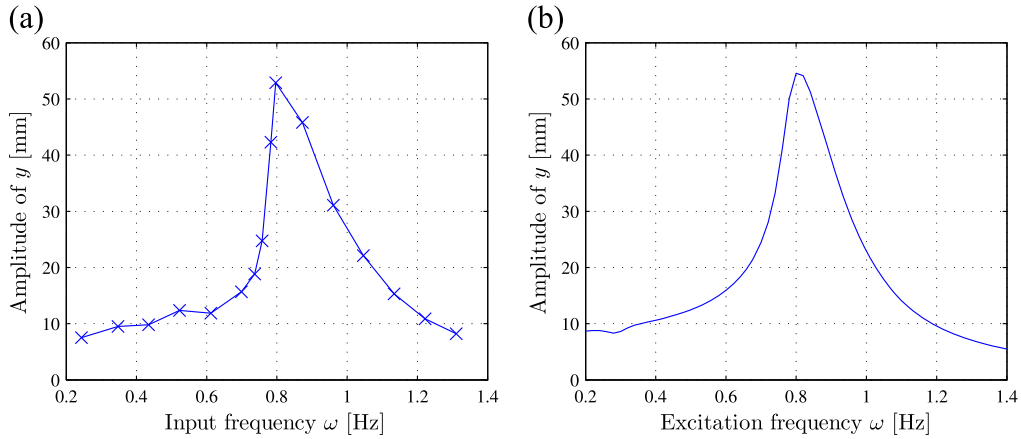

Figure 13. Experimentally obtained (a) and numerically simulated (b) frequency responses. The excitation amplitude is $A = 61$ mm $(0.9l_0)$, and in the numerical simulations, the pre-tension is $x_0 = 630$ mm $(1.6l_0)$ and the temperature is $T = 23$ °C. In experiments, the quantities are estimated to be the same.

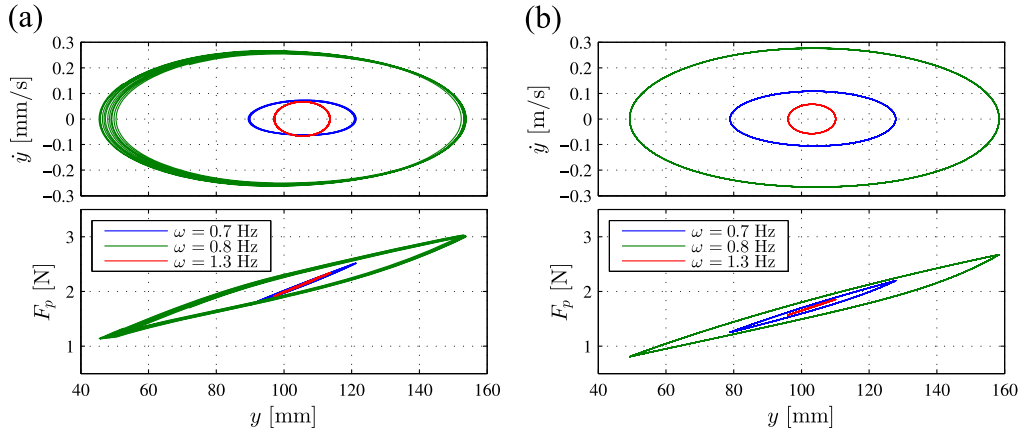

Figure 14. State space and PE spring force at several oscillator frequencies in experiment (a) and numerical simulation (b). In the numerical simulations, the pre-tension is $x_0 = 630$ mm $(1.6l_0)$, and the temperature is $T = 23$ °C. In experiments, the quantities are estimated to be the same.

a thread (see figure 1(b)). Initially, a frequency response is performed, and later the effects of changing temperature are analysed.

6.1. Constant temperature

The frequency response analysis is done by considering the system steady state responses for specific forcing frequencies. This analysis is done by inducing oscillations at different frequencies. After the steady state is reached and the reading has been performed, the system is stopped and then a new frequency is analysed.

Figure 13 presents the experimental and modelled frequency response. The experimental analysis points to a resonance frequency around 0.8 Hz $(0.92\omega_0)$, being associated with a non-symmetric peak, which is well reproduced in simulation. The lower side of the resonance peak is steeper in experiments than in simulation.

Figure 14 shows the PE spring force and the state space for three oscillator frequencies: below, at, and above the resonance condition. It is important to observe that the system response at resonance is related to the great amount of energy dissipation due to hysteresis. In the experiments, the equilibrium point changes within 5 mm $(0.08l_0)$ with varying frequencies, which is in agreement with the movement of the equilibrium point investigated earlier. This is, however not reproduced in simulation, where the centre of oscillations is constant. Again, the simulated oscillation amplitudes are higher than measured right below resonance, i.e., at 0.7 Hz.

In experiments, the change in amplitude from measurement to measurement is large just below resonance ($\omega \in [7.5; 8]$ Hz). This could indicate a bifurcation, where the dynamic state jumps from one attractor to another. As mentioned in the Introduction, such behaviour has been detected in SMA dynamic systems before and has been reported in the literature (e.g., Sitnikova *et al* (2012)). Nevertheless, coexisting attractors have not been detected based on several tests of frequency sweeps around the resonance peak both experimentally and numerically.

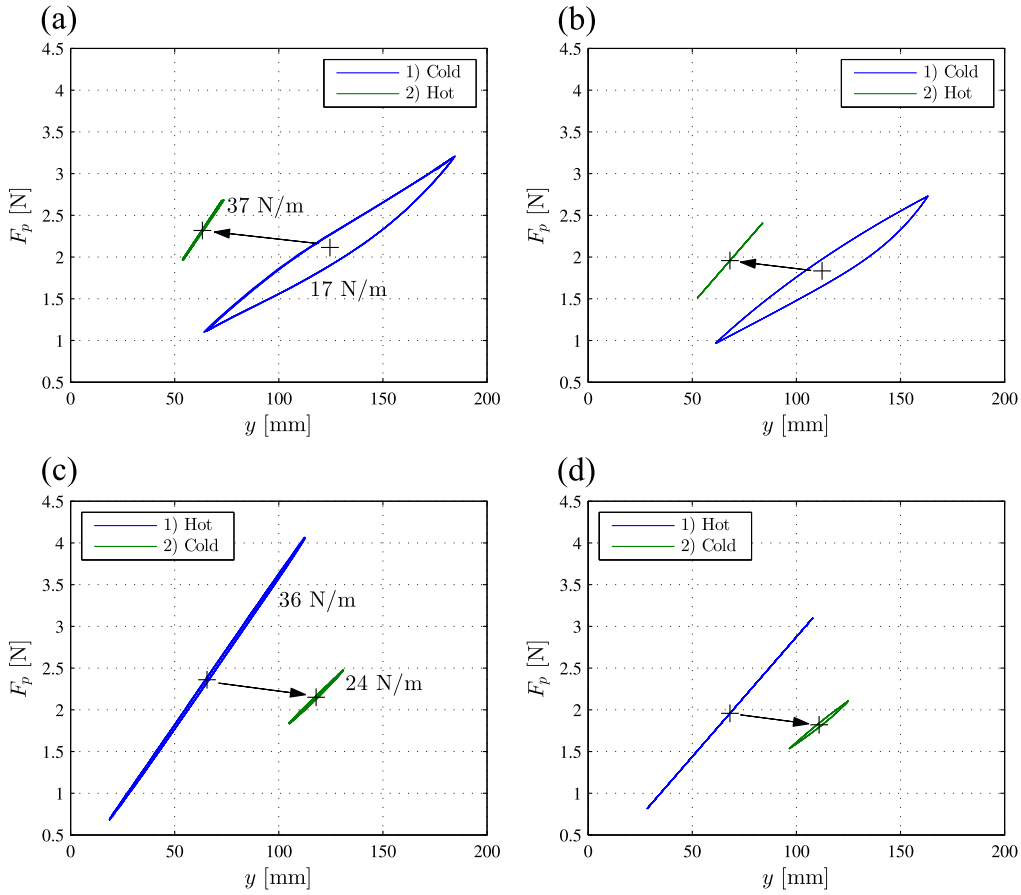

Figure 15. Experimental and simulated forced steady state responses. (a) and (c) Experiments at $\omega = 0.8$ Hz and $\omega = 1.2$ Hz, respectively; (b) and (d) simulations at $\omega = 0.8$ Hz and $\omega = 1.2$ Hz, respectively. In experiments, the spring is heated by a 1.0 A current. In simulation, the temperature changes between $T = 23$ °C and $T = 80$ °C; the pre-tension is $x_0 = 670$ mm ($1.7l_0$). The excitation amplitude is in both cases $A = 61$ mm ($0.9l_0$).

6.2. Varying temperature

At this point, forced vibrations with temperature variations are investigated. This analysis is of special interest in terms of vibration reduction. Tests consider heating and cooling processes, defining two different conditions: hot and cold. Two forcing frequencies are evaluated.

The first case starts at room temperature close to a resonance condition. After the steady state is reached, the spring is heated, and this condition is held constant until a new steady state is reached. Results for this test and the related simulation are shown in figures 15(a) and (b). At room temperature, the peak-to-peak amplitude is 122 mm ($1.88l_0$) and the average stiffness is 17 N m^{-1} ($0.85k_0$) in experiments. When the temperature is increased, the cart moves 61 mm ($0.94l_0$) to the left, the peak-to-peak amplitude is decreased to 20 mm ($0.15l_0$), and the stiffness is increased to 37 N m^{-1} ($1.9k_0$). Because of the increasing stiffness due to the rising temperature, the system resonance frequency increases and moves away from the excitation frequency. This means, that it is beneficial in terms of vibration reduction to heat the PE spring to increase the stiffness at this forcing condition at room temperature. However, it is important to highlight that when heating the spring to increase the stiffness, the dissipative characteristics due to hysteresis are sacrificed. Phase transformations cannot occur in large scale at high temperatures. This case highlights the trade-off between a beneficial stiffness increase and an unfavourable hysteresis decrease. The same qualitative behaviour is seen in simulation. The quantitative properties are, however, slightly different; e.g., the stiffness at high temperature and the distance between the equilibrium positions due to the temperature change. This is primarily because the force-displacement relationship of the spring in the hot condition is not captured perfectly; the stiffness is too low; cf figure 6.

In the second case, seen in figures 15(c) and (d), the system is started in a hot condition around its resonance frequency and later is cooled down to room temperature. At high temperature, the peak-to-peak amplitude is 94 mm ($1.44l_0$) and the stiffness is 36 N m^{-1} ($1.8k_0$). No significant hysteresis occurs at this temperature, even though the amplitudes are large. When cold, the peak-to-peak amplitude is reduced to 28 mm ($0.44l_0$), with an average stiffness of 24 N m^{-1} ($1.2k_0$) in experiments. Still, the amount of hysteresis is negligible, and this time the reason is the low vibration amplitudes. This means that in this case, both stiffness and

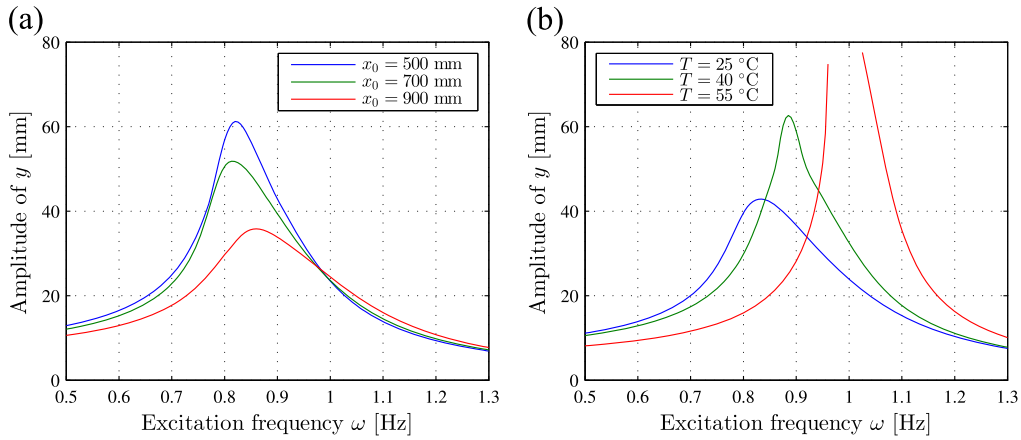

Figure 16. Theoretical frequency response functions of the system under different conditions. (a) Different levels of pre-tension. The temperature is $T = 25$ °C. (b) Distinct temperatures. The pre-tension is $x_0 = 800$ mm $(2.0l_0)$.

hysteresis changes are beneficial, even though the major improvements are due to the stiffness changes alone, and the increase in hysteresis is insignificant. Note, however, that the change in stiffness is less than it is in the first case because the amplitude in the cold case is smaller, which gives a higher average stiffness. In simulation the behaviour is similar. However, because the high temperature stiffness is lower than in experiments, an excitation frequency of 1.1 Hz has been chosen instead of 1.2 Hz to get closer to the resonance condition.

For the two cases, it is concluded that a shift in temperature causes changes in both stiffness and hysteresis. Generally the stiffness is the most dominant factor in terms of system dynamics. Furthermore, there is a trade-off; a beneficial stiffness change might cause unfavourable loss of hysteresis, which appears only at low temperatures and high amplitudes.

7. Vibration reduction—theoretical model application

The theoretical model presented has been shown to be appropriate to match experimental data related to pseudoelastic SMA systems with high accuracy. Results presented in sections 4, 5, and 6 reinforce this argument, and therefore, it can be applied to investigate situations related to vibration reduction. In this regard, two numerical investigations are carried out, evaluating the influence of pretension and temperature changes. Figure 16 shows results related to frequency response analysis for different levels of pretension and temperatures. Note that the pretension level does not influence the resonance frequency but has a significant influence on energy dissipation because it promotes changes in hysteresis. On the other hand, the temperature of the SMA element has a significant influence on the resonance condition due to stiffness change. Note that the resonance frequency is changed 20% relative to the cold case. Both situations can be employed for vibration reduction purposes.

The change in resonance frequency can be exploited to avoid critical situations. For instance, it is possible to pass through critical speeds reducing transient vibration amplitudes with the use of active temperature variations. Nevertheless, there is a trade-off between stiffness and hysteretic changes, in the sense that the level of energy dissipation is also changed by temperature variations; cf figure 15. At 55 °C, there is a region around resonance ($\omega \in [0.96; 1.03]$ Hz), where the energy dissipation capabilities are so low that the vibration amplitude becomes higher than the pretension of the PE spring, causing the spring and the connecting threads to become loose (not in tension) at certain instants in the oscillation cycle. This state of motion involves unwanted complex dynamic behaviour. This means that high-temperature conditions are useful and safe only when the excitation frequency is far away from the resonance frequency.

8. Conclusions

Experimental and theoretical analyses are carried out for a one degree of freedom oscillator with a pseudoelastic SMA element. The system investigation shows complex nonlinear behaviour due to the intricate thermo-mechanical relations of the pseudoelastic shape memory alloy spring. Brinson's model is employed for the thermo-mechanical description of the SMA spring, and two modifications have been presented: hardening and sub-loop functions. These modifications allow very good agreement with experimental data obtained either for quasi-static or dynamical situations. Equilibrium positions are investigated, showing that they strongly depend on the initial condition of the cart (position, velocity, and martensitic volume fraction) at room temperature. The equilibrium position varies up to 50% of the initial SMA spring length. Moreover, it significantly depends on the temperature, where variations are up to 150%. By heating the pseudoelastic spring when the cart is in equilibrium, the cart starts moving in a jagged fashion, which is caused by a competition between compliance (due to a forward phase transformation) and stiffening (due to temperature increase). Similar behaviour can be achieved when cooling the spring. Pretension of the SMA spring is investigated, showing its influence on

energy dissipation induction and hysteretic behaviour (vibration amplitudes reduced 50% at resonance for high-level compared with low-level pretension). Temperature variations are also investigated, showing the possibility of inducing stiffness change due to phase transformation associated with temperature variations. At high temperatures, the spring behaves linearly elastically, which means that the spring consists of pure austenite. Essentially, it is important to point out the trade-off between both aspects, stiffness and hysteresis, in order to define system dynamics. Strong vibration reduction can be achieved using SMA elements.

Acknowledgments

The authors would like to thank the Danish Ministry of Science, Innovation and Higher Education for the support to FTP Research project 12-127502, as well as the Brazilian research agencies CNPq, CAPES, and FAPERJ and, through the INCT-EIE (National Institute of Science and Technology—Smart Structures in Engineering), CNPq and FAPEMIG for their support. The Air Force Office of Scientific Research (AFOSR) is also acknowledged.

References

Aguiar R A A, Savi M A and Pacheco P M C L 2010 *Smart Mater. Struct.* **19** 025008
Aguiar R A A, Savi M A and Pacheco P M C L 2013 *J. Intell. Mater. Syst. Struct.* **24** 247–61
An S M, Ryu J, Cho M and Cho K J 2012 *Smart Mater. Struct.* 21
Bekker A and Brinson L 1998 *Acta Mater.* **46** 3649–65
Bernardini D and Rega G 2011 *Int. J. Bifurc. Chaos Appl. Sci. Eng.* **21** 2769–82
Bernardini D and Rega G 2011 *Int. J. Bifurc. Chaos Appl. Sci. Eng.* **21** 2783–800
Brinson L C 1993 *J. Intell. Mater. Syst. Struct.* **4** 229–42
Brinson L C and Huang M S 1996 *J. Intell. Mater. Syst. Struct.* **7** 108–18
Budynas R and Nisbett J 2008 *Shigley's Mechanical Engineering Design* 8th edn (New York: McGraw-Hill) pp 500–39
Cartmell M P, Żak A J and Ganilova O A 2012 *Nonlinear Dynamic Phenomena in Mechanics* (*Solid Mechanics and Its Applications* vol 181) ed J Warminski, S Lenci, M P Cartmell, G Rega and M Wiercigroch (Dordrecht: Springer) pp 115–58
dos Santos B C and Savi M A 2009 *Chaos Solitons Fractals* **40** 197–209
Enemark S, Savi M A and Santos I F 2014 *Smart Struct. Syst.* at press
Furst S J and Seelecke S 2012 *J. Intell. Mater. Syst. Struct.* **23** 1233–47
Janke L, Czaderski C, Motavalli M and Ruth J 2005 *Materials and Structures* **38** 578–92
Lagoudas D C (ed) 2008 *Shape Memory Alloys: Modeling and Engineering Applications* (New York: Springer) pp 171–80
Lagoudas D, Hartl D, Chemisky Y, Machado L and Popov P 2012 *Int. J. Plasticity* **32-33** 155–83
Liang and Rogers 1990 *J. Intell. Mater. Syst. Struct.* **1** 207–34
Machado L G, Lagoudas D C and Savi M A 2009 *Int. J. Solids Struct.* **46** 1269–86
Mirzaeifar R, DesRoches R and Yavari A 2011 *Int. J. Solids Struct.* **48** 611–24
Monteiro Paulo Cesar C J, Savi M A, Netto T A and Pacheco P M C L 2009 *J. Intell. Mater. Syst. Struct.* **20** 1675–87
Nagaya K, Takeda S, Tsukui Y and Kumaido T 1987 *J. Sound Vib.* **113** 307–15
Paiva A and Savi M A 2006 *Math. Prob. Eng.* **2006** 56876
Phillips J W and Costello G A 1972 *J. Acoust. Soc. Am.* **51** 967–73
Savi M A, de Paula A S and Lagoudas D C 2011 *J. Intell. Mater. Syst. Struct.* **22** 67–80
Silva L C, Savi M A and Paiva A 2013 *J. Sound Vib.* **332** 608–21
Sitnikova E, Pavlovskaia E, Ing J and Wiercigroch M 2012 *Smart Mater. Struct.* **21** 075028
Williams K A, Chiu G T C and Bernhard R J 2002 *Proc. SPIE* **4701** 200–13